Editors' Suggestion

Ferroelastically protected polarization switching pathways to control electrical conductivity in strain-graded ferroelectric nanoplates

Kwang-Eun Kim,[1] Yong-Jin Kim,[1] Yang Zhang,[2,3] Fei Xue,[2] Gi-Yeop Kim,[4] Kyung Song,[5] Si-Young Choi,[4,5] Jun-Ming Liu,[3,6] Long-Qing Chen,[2] and Chan-Ho Yang[1,7,*]

[1]*Department of Physics and Center for Lattice Defectronics, Korea Advanced Institute of Science and Technology, Yuseong-gu, Daejeon 34141, Republic of Korea*

[2]*Department of Materials Science and Engineering, The Pennsylvania State University, University Park, Pennsylvania 16802, USA*

[3]*Laboratory of Solid State Microstructures, Nanjing University and Innovation Center of Advanced Microstructures, Nanjing 210093, People's Republic of China*

[4]*Department of Materials Science and Engineering, POSTECH, Pohang, Gyeongbuk 37673, Republic of Korea*

[5]*Department of Materials Modeling and Characterization, Korea Institute of Materials Science, Changwon, Gyeongnam 51508, Republic of Korea*

[6]*Institute for Advanced Materials, South China Academy of Advanced Optoelectronics and Guangdong Provincial Laboratory of Quantum Engineering and Quantum Materials, South China Normal University, Guangzhou 510006, People's Republic of China*

[7]*Institute for the NanoCentury, Korea Advanced Institute of Science and Technology, Yuseong-gu, Daejeon 34141, Republic of Korea*

(Received 9 June 2018; published 27 August 2018)

Controllable local electronic conduction in otherwise insulating materials can be created by arranging two opponent ferroelectric polarizations in a head to head (or tail to tail) configuration. Using an effective trailing field of dc biased tip motion, charged domain walls have been artificially created in the context of tip-based nanolithography. However, the charged domain wall formed by a trailing field is unstable because of elastic interaction at the boundary between poling and nonpoling regions, finally resulting in ferroelastic back-switching. Here, we report that nanoscale plate structures under strain relaxation can provide a promising opportunity for stabilization and manipulation of a charged domain wall using a highly anisotropic mechanical boundary condition that restricts the unique ferroelastic domain configuration. We demonstrate that a ferroelectric $BiFeO_3$ nanoplate subjected to compressive misfit strain at the bottom but less external stress on the side walls exhibits radial-quadrant in-plane ferroelectric domain structures. Electronic conduction is significantly enhanced near the side walls and the magnitude of electrostatic conductivity is adjustable up to about 20 times by 180° ferroelectric switching that is protected by the clamped ferroelastic domain. Our findings provide a pathway to controllable nanoelectronic logic devices by tuning a charged ferroelectric domain wall.

DOI: 10.1103/PhysRevMaterials.2.084412

I. INTRODUCTION

Significant research interest has been dedicated to ferroelectric domain walls as conductive channels for future nanoelectronic devices due to their advantages of nanometric size and modifiability of location and polarity [1]. For domain-wall conduction, intriguing mechanisms have been suggested, including polarization discontinuity [2,3], topological structures [4–6], and defect accumulation [7,8] in ferroelectric two-dimensional thin layers and bulk compounds. However, charged domain walls (CDWs) have rarely been observed in ferroelectric nanostructures because of the large domain-wall energy [9], and thus a single domain structure has been predicted to be the probable configuration. Ferroelectric nanostructures are distinct from bulk or thin-film materials because their side walls undergo less external stress in contrast to the bottom interface [10,11], which is clamped by the substrate through misfit strain. This asymmetric stress can generate a deformation of shape under a large strain gradient associated with fast strain relaxation, which gives rise to the flexoelectric effect [12–15]. Moreover, as stress is directly coupled to the ferroelastic state, asymmetric strain engineering through control of the nanoplate shape can stabilize CDWs by limiting possible ferroelectric domain structures. To implement this capability, it is necessary to make a nanoplate system with a strong compressive or tensile strain imposed on its bottom interface to induce fast strain relaxation.

Recent reports have featured artificially constructed CDWs that show significant conductivity enhancement in comparison with the insulating bulk domain [16–19]. One of the methods to stabilize and manipulate CDWs in ferroelectric materials is to employ a biased atomic force microscope (AFM) tip. When a positive (negative) voltage is applied to the tip, rotationally symmetric electric fields diverge (converge) at the tip. The lateral motion of a biased tip breaks the symmetry of the electric fields and creates a net in-plane (IP) electric field (called the trailing field). The biased AFM tip stabilizes the CDWs via two effects: a trailing field effect of the dc biased tip motion to control the IP polarization component and electron injection

*Corresponding author: chyang@kaist.ac.kr

from the tip during the poling procedure to compensate for the polarization charge [20–23]. However, CDWs artificially constructed by the dc biased tip are generally unstable because of elastic interaction along the boundaries of the poled area, after which ferroelastic back-switching occurs at zero electric field over time [24]. Furthermore, the CDWs for nanoelectronic applications should be structurally stable, without implanted free carriers, and easily controllable by a fixed top-bottom electrode geometry rather than using a trailing field.

In this paper, we present an exotic ferroelectric quadrant domain structure where each quadrant domain has an outward in-plane polarization forming an unchiral vortex point at the central point. This electrostatically unstable domain structure can be emergent by radial misfit strain relaxation of the nanoplate, which restricts ferroelastic domain configuration and inevitably creates the charged ferroelectric domain structure. We demonstrated a strain-graded ferroelectric nanoplate using the prototypical ferroelectric $BiFeO_3$ (BFO). BFO has a G-type antiferromagnetism ($T_N \sim 640$ K) and ferroelectricity ($T_C \sim 1103$ K) with a rhombohedral structure [25,26]. The spontaneous ferroelectric polarization of BFO is $\sim 100\,\mu C\,cm^{-2}$ along the pseudocubic ⟨111⟩ direction in weakly strained epitaxial films [27].

In the following, we not only reveal the charged ferroelectric domain structure by using vector piezoresponse force microscopy (PFM), but we also investigate local electronic conductivity of the BFO nanoplate by using conductive atomic force microscopy (c-AFM). We report that significant electronic conduction occurs near the edge of a ferroelectric nanoplate and the enhanced electronic conduction can be suppressed by 180° polarization switching in a reversible way. We discuss a possible mechanism of the conduction modulation on the basis of screening of the bound charges and junction charge injection.

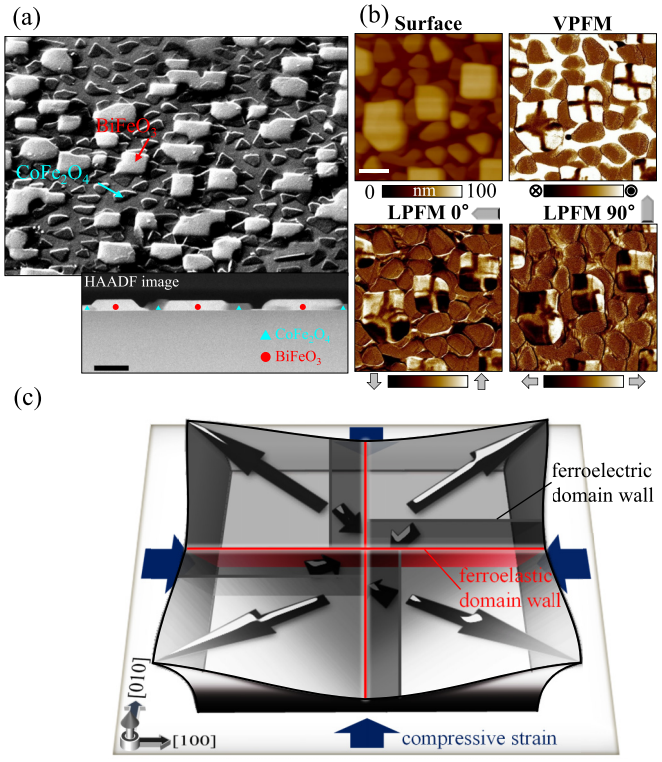

FIG. 1. (a) A 55° tilted SEM top view image clearly showing BFO and CFO phase separation. In many cases, BFO nanoplates have 400–500-nm lateral sizes with ~60-nm height, as shown in the inset TEM image. The scale bar of the inset figure represents 200 nm. (b) PFM images showing domain structures of BFO nanoplates in the as-grown state. LPFM 0 and 90° images are measured at 90° different cantilever orientations, as illustrated by the drawing. The scale bar represents 400 nm. (c) Schematic illustration showing the quadrant and buffer domain forming process.

II. EXPERIMENTAL RESULTS

A. Exploring BFO nanoplate structures under strain relaxation

BFO nanoplate structures were designed by $BiFeO_3$-$CoFe_2O_4$ (BFO-CFO) self-assembly growth on a (001) $LaAlO_3$ (LAO) substrate with a bottom electrode $Pr_{0.5}Ca_{0.5}MnO_3$ (PCMO) layer. Because of the large difference in lattice constants, the CFO and BFO grow into individual nanostructures without mixing [28]. The BFO (001) and the CFO (111) structures were identified by x-ray-diffraction peaks (Fig. S1 in the Supplemental Material [29]). In the scanning electron microscopy (SEM) image, the squared and protruding BFO nanoplates are surrounded by triangular CFO clusters [Fig. 1(a)]. In the high-angle annular dark-field (HAADF) transmission electron microscopy (TEM) image, the BFO shares boundaries with the CFO, which can affect the electronic conductivity by forming a heterojunction. We will discuss the influence of the heterojunction on the electronic conductivity later in this paper.

To investigate the ferroelectric domain structures in detail, we performed vector PFM measurement [Fig. 1(b)]. The lateral PFM (LPFM) technique distinguishes only the perpendicular component of the piezoresponse vector with regard to the cantilever orientation by the torsional vibration mode. In order to construct the distribution of the IP piezoresponse vectors, two LPFM images measured at 90° different cantilever orientations are required to distinguish the four IP polarization variants because BFO has a rhombohedral structure elongated along a ⟨111⟩ axis [30]. From the vertical PFM (VPFM) and LPFM images, the domain structure of the BFO nanoplates can be divided into two parts: one is the quadrant domain with outward/upward polarizations, and the other is the cross-shaped buffer domains with inward/downward polarizations. Details of the BFO domain structure were double checked by angle-resolved PFM, as shown in Fig. S2 in the Supplemental Material [29]. Figure 1(c) depicts a possible scenario for a domain forming process of the BFO nanoplate. The bottom interface of the BFO nanoplate is under compressive strain due to large lattice mismatch with the LAO substrate; also, because the top and side surfaces are stress free, the BFO nanoplate undergoes radial strain relaxation. The strain relaxation behavior is confirmed in the x-ray reciprocal space map, in which the BFO peak has a diffusive feature (Fig. S1 in the Supplemental Material [29]). The radial strain relaxation results in inhomogeneous shear strain within the BFO nanoplate, and the four variant ferroelastic domains of the rhombohedral BFO are stabilized along corresponding shear strain deformations. Upward polarizations in the quadrant domain have their origin in a

flexoelectric field formed by compressive strain relaxation; slim buffer domains with downward polarizations are interposed between two ferroelastic domains to reduce depolarization energy. Details of strain depth profiles and strain cross sectional maps calculated by the phase field simulation are represented in Ref. [31]. From the phase field simulation [31], we confirm that ε_{11} and ε_{22} show the large strain gradient with respect to the sample thickness direction at the four corners. The flexoelectric tensor f_{3311} and f_{3322} produce an upward flexoelectric field, resulting in a net upward polarization in the as-grown state. The size of the buffer domains is determined by the competition between the flexoelectric and depolarization fields. Similar quadrant domains are commonly observed in almost all nanoplates regardless of the size and shape, as shown in Fig. 1(b). The radial quadrant domain structure is a type of CDW in which free-electron carriers are concentrated along nanoplate side edges and screen the positive bound charges of polarizations.

B. Domain control by 180° polarization switching

Controlling polarization is an essential step to manipulate the charge carrier density on the CDWs, but controlling the ferroelectric domain at the size of several hundred nanometers is a challenging assignment. In the BFO nanoplate case, this problem is tackled just by switching the out-of-plane (OOP) component of the polarization, which spontaneously leads to the reversal of the IP polarization component. In Figs. 2(a) and 2(b), OOP polarization switching results in 180° ferroelectric switching due to the mechanical clamping of ferroelastic elongation along the ⟨111⟩ axis, as shown in the schematic illustration below in Fig. 2. As a result, when we apply an OOP electric field across the BFO nanoplates, the asymmetric mechanical boundary condition limits possible ferroelectric domain structures and allows only two types of domain configuration, the outward/upward radial quadrant domain (ORQD) structure and the inward/downward radial quadrant domain (IRQD) structure. The as-grown ORQD state can be switched into IRQD and vice versa by additional polarization switching [red box in Fig. 2(c)]. Although we used a dc biased tip to switch the electric polarization, this was done only to apply an OOP electric field and differs from the trailing field method, which involves scanning in the opposite slow scan directions. Compared to the trailing field method, 180° ferroelectric switching in the rhombohedral structure has an advantage for applications in nanoelectronic devices because the carrier type at the CDW is easily adjustable by using an OOP electric field in top-down capacitor geometry. In the ORQD (IRQD) structures, positive (negative) bound charges are in the vicinity of side walls, and as a result n-type (p-type) free carriers are attracted to the side walls to screen the bound charges of polarizations. The redistribution of free carriers is presumed to lead to the nonuniform distribution of electronic conductivity. In the following current measurements, to avoid a complicated interpretation process, we take no regard of the buffer domain effect because the buffer domain occupies only a small fraction of the nanoplate edges.

C. Local conductivity measurement in the double box switching area

To illustrate the relation between the domain type and the electronic conductivity, we measured the current map using

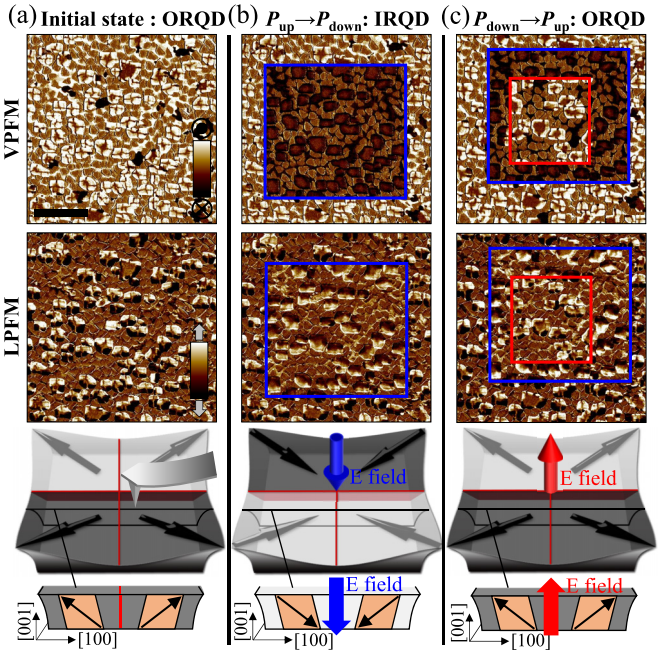

FIG. 2. Large area VPFM and LPFM images and schematic illustration of the domain configuration for (a) the initial state, (b) the OOP switching state from upward to downward polarization, and (c) an additional switching state from downward to upward polarization with a box-in-box pattern. The blue box and red box areas are scanned by a dc biased tip at +3 and −3 V, respectively. During the OOP polarization switching process, the LPFM signal is reversed between the outward and inward piezoresponse orientations, indicating a strong coupling between OOP and IP polarizations. Compared to the as-grown state, most BFO nanoplates show the reversible nature of polarization switching. Colors in the schematic of the domain configuration reflect LPFM signals. The scale bar represents 2 μm.

c-AFM in the box-in-box domain switching area (Fig. 3). By measuring ORQD and IRQD types in a single scan, crucial uncontrollable issues raised by the tip contact condition can be eliminated [32]. Moreover, a statistical approach is also possible by measuring many nanoplates at once. The measured region is divided into three parts: the as-grown ORQD state (outermost region), the switched IRQD in the downward polarization region (blue box), and the returned ORQD in the upward polarization region (red box). Figure 3(d) clearly shows the current increase in the ORQD structures compared to the IRQD. A slight difference in conductivity is observed because of the different sizes and shapes of the BFO nanoplates due to self-assembly growth, but it is clear that a high current in most nanoplates is formed in the ORQD structure. Figures 3(e), 3(f), and 3(g) provide current images of the representative nanoplates in each area. Considering the side wall of the nanoplate in the AFM deflection error image, the enhancement of electric current can be seen not to occur exactly along the edge but to occur inside the edge. This result suggests that the enhancement of current is not directly attributed to possible topographic crosstalk and/or defect accumulation at the heterointerface between the BFO and CFO [33].

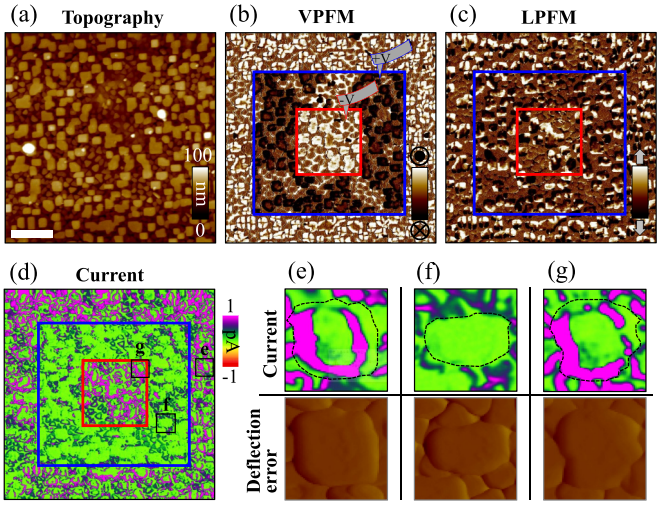

FIG. 3. (a) Surface, (b) VPFM, (c) LPFM, and (d) current images measured on the double box switching area. The scale bar represents 2 μm. Enlarged current images representing nanoplates acquired at (e) ORQD (outermost area), (f) IRQD (blue box), and (g) ORQD (red box) areas. Edges of BFO nanoplates are depicted by dotted lines obtained from deflection error images.

D. Electrical conductivity of the ORQD and IRQD domain configurations

Figure 4(a) shows the change of the electrical conductivity according to the domain type in a nanoplate. A significant current enhancement is measured in the ORQD structure inside the side wall of the nanoplate (the side wall is marked by a black line). The high conduction toward the nanoplate lateral edge (red arrow) is caused by the effect of the ferroelastic domain wall. We measured the I-V curves at two representative positions for ORQD and IRQD types, as marked in Fig. 4(a) (red and black points). The sweep range of the voltage is up to $\pm$ 2.5 V, considering a coercive voltage of $\pm$ 3 V to avoid complex phenomena related to polarization switching. Figure 4(b) clearly shows that the electronic conduction in the ORQD is approximately ~20 times higher than that in the IRQD. The I-V curve of the ORQD exhibits Schottky diode behavior with a forward direction at a positive sample voltage, while the IRQD has a symmetrical I-V curve, as shown in the inset, which is plotted at logarithmic scale. The Schottky diode behavior in the ORQD structure is caused by the difference of Schottky barrier heights between PCMO/BFO and BFO/Pt junctions [Fig. 5(b)]. The Schottky barriers are determined by the following information: the work functions of PCMO and Pt are 4.9 and 5.65 eV [34,35], and the electron affinity and the band gap of the BFO are 3.3 and 2.7 eV, respectively [36]. In the ORQD structure with the upward electric polarization, the bound charge of the polarization changes the Schottky barrier by 1.38 eV [36], and this determines the direction of electron flow from the low to high Schottky barrier, as shown in Fig. 5(b). In order to characterize the conduction mechanism, I-V curves measured with a positive sample voltage have been plotted within a Schottky emission ($\ln I \sim V^{1/2}$) model [37], as shown in Fig. S3 in the Supplemental Material [29]. In ORQD and IRQD structures, both data have been

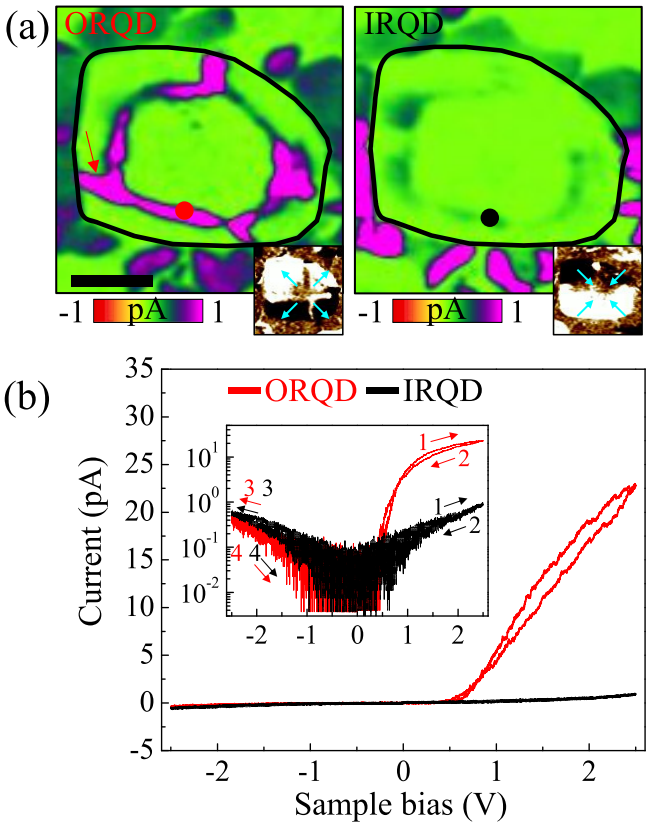

FIG. 4. (a) c-AFM current maps of ORQD and IRQD types. Black lines represent edges of nanoplates. Insets are LPFM images and arrows depict IP polarization vectors. The scale bar represents 200 nm. (b) I-V curves taken for both ORQD (red lines) and IRQD (black lines) at representative positions shown in panel (a). A graph of logarithmic scale showing details of I-V curves is shown in the inset. Arrows represent the bias sweep direction.

linearly plotted within the framework of the Schottky emission, and the curve is saturated for higher current in the ORQD structure.

To explain the electric conductivity enhancement inside the edge of the nanoplates in the ORQD structure, a scenario is proposed based on the band diagram, as summarized in Fig. 5(c). Because the CFO has a smaller band gap than that of BFO [38], the band of BFO doped with n-type carriers bends downward. In the ORQD structure, the band goes down from the center to the edge because of the bound charge of the outward polarization. Since screening charges absorbed from air and the bottom electrode are concentrated at the nanoplate center where bound charges are focused, the band at the central region becomes gentle. The location of the lowest conduction-band minimum is inside the edge due to the competition between the Schottky interfacial effect and the polarization bound charge effect, thereby leading to the current enhancement inside the edge. Meanwhile, in the IRQD structure, the band goes up from the center to the edge because of the bound charge of the inward polarization. Because of the gentle slope of the band at the nanoplate center, the free electrons are spread over a wide area and the conductivity is not significantly increased.

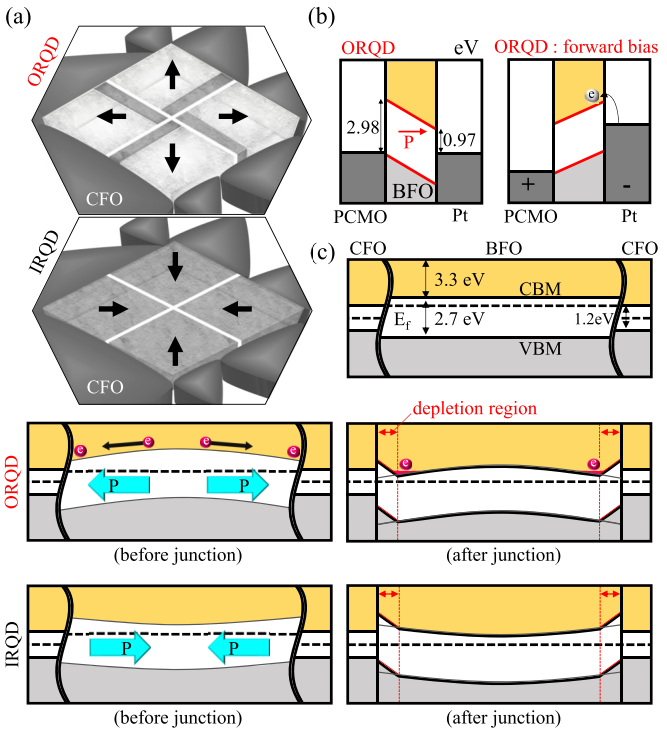

FIG. 5. Schematic illustrations of electronic band structures of a BFO nanoplate. (a) Schematics describing ORQD and IRQD structures surrounded by CFO. Arrows represent IP polarizations. (b) Electronic band structure to explain Schottky diode behavior. The BFO/Pt interface has a smaller Schottky barrier than the BFO/PCMO interface due to bound charges of electric polarization in the ORQD structure. The forward bias is determined by the difference of Schottky barriers to the flow of electrons from Pt to PCMO. (c) Electronic band bending of the BFO nanoplate by Schottky effect and bound charge of electric polarization. Because the BFO has a higher Fermi energy level than the CFO, the BFO band bends down to match the Fermi energy levels when the BFO bonds to the CFO at the side interface. In the ORQD (IRQD) type, the electronic energy level increases (decreases) at the center and decreases (increases) at the side edge of the BFO nanoplate due to electric polarization.

E. Phase field simulation

To verify the above scenario for the origin of electronic conduction in the BFO nanoplate, we performed phase field simulations. To describe the domain structures in BFO, the total free-energy density includes the bulk energy, gradient energy, elastic energy, and electrostatic energy. A more detailed form of the model can be found in the Methods section. The bound charges at the top surface and bottom interface of BFO can be compensated by screening charges absorbed from air and the bottom electrode, respectively [39]. To describe the screening effect, we calculate the bound charges from the discontinuity of polarization, and add screen charges with a negative sign, to guarantee that the total density of charges at the top surface and bottom interface is zero. The electrostatic potential φ is calculated by solving the Poisson equation (the reference of the electric potential has been set to be the average potential over the whole nanoplate), and the electrical conductivity in the BFO nanoplate is approximated based on the Boltzmann statistics [40]:

$$\sigma = N_0 e \mu \exp\left(-\frac{e\varphi}{k_B T}\right), \tag{1}$$

where N_0 is the carrier density of the bulk BFO, e is the charge of an electron, μ is the carrier mobility, k_B is the Boltzmann constant, and T is the absolute temperature.

First, only the bound charge from polarization is considered in the simulations. In ORQD (IRQD) types, n-type (p-type) carriers move to the side wall to compensate for the positive (negative) bound charge. In the ORQD structure, the highest electrostatic potential is formed at the side wall by the positive bound charge. Since n-type free carriers are dominant in BFO, the conductivity is increased along the side wall [Fig. 6(a)]. On the other hand, in the IRQD case, a high electrostatic potential is formed at the center and ferroelastic domain walls by the positive bound charge of the polarization [Fig. 6(c)]. Therefore, if we only incorporate the influence of the bound charges, the experimental observation cannot be satisfactorily explained.

Next, junction space charges are artificially added in the phase field simulations to depict the Schottky barrier which arises due to the difference of electronic band structures between BFO and CFO [Fig. S4(a) in the Supplemental Material [29]]. Due to the difference of the chemical potentials between the BFO and CFO, positive and negative space-charge regions are formed near the boundaries of BFO and CFO [Fig. S4(b) in the Supplemental Material [29]]. The junction space charges affect the distribution of the electrostatic potential, and the highest potential and thus the highest conductivity occur inside the side wall for the ORQD case [Fig. 6(b)], which is consistent with the experimental observations. For the IRQD case, after considering the junction space charges, the high electrostatic potential region spreads out evenly in the nanoplate, so that the high conductivity at the center of the nanoplate disappears [Fig. 6(d)]. Although the electronic conductivity at the four point regions is enhanced, as shown in Fig. 6(d), these were difficult to observe in the experiment due to their small size.

III. METHODS

A. Growth of the BFO nanoplate structure

BFO-CFO nanostructures were grown by pulsed laser deposition using a single target composed of $0.65Bi_{1.1}FeO_3$ and $0.35CoFe_2O_4$. The 10% bismuth excess was used to compensate for the bismuth volatility. The films were deposited using a krypton fluoride (KrF) excimer pulsed laser (Coherent, COMpex Pro 205F) with a wavelength of 248 nm and focused spot size of ~4 mm^2. An incident laser on the surface of a target was used at a fluence of 0.8 J cm^{-2} with a frequency of 7 Hz. Growth was performed at 630 °C under an oxygen environment of 100 mTorr. After the growths were completed, the samples were cooled to room temperature at a rate of 10 °C min^{-1} under an oxygen environment at 500 Torr. The BFO-CFO self-assembled structures were deposited on (001)-oriented LAO single crystal substrates with a bottom electrode (~4 nm thick) of PCMO.

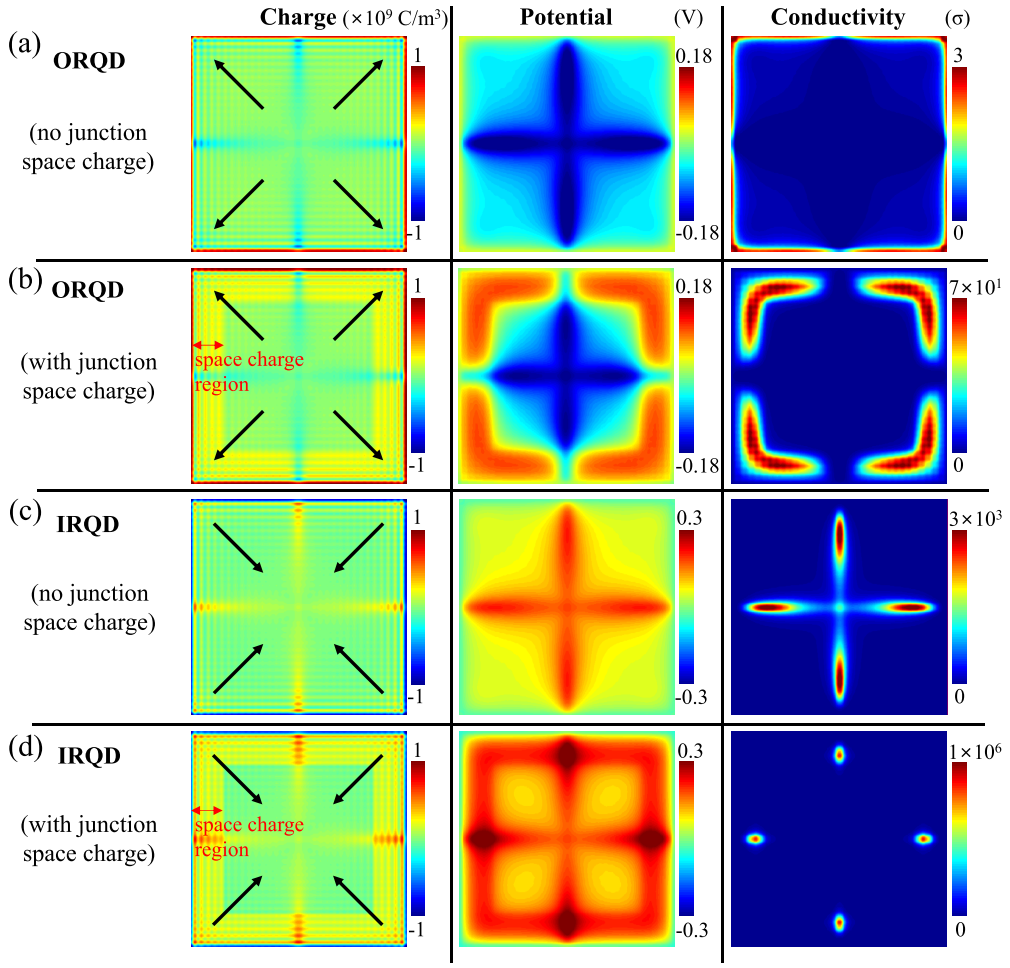

FIG. 6. Phase field simulations of the electronic conductivity for the ORQD and IRQD domain configurations with and without junction space charges. (Left) Average charge density map along the OOP direction, (middle) corresponding electrostatic potential, and (right) electronic conductivity on the top surface of the BFO nanoplate for the ORQD structure without/with junction space charges (a), (b), and for the IRQD structure without/with junction space charges (c), (d). In the ORQD structure, the space charge forms a high electrostatic potential region inside the nanoplate side wall. In the IRQD structure, the electrostatic potential is enhanced in the space-charge region, reducing the electrostatic potential in the center of the nanoplate. Red arrows indicate the positive space-charge regions within BFO.

B. PFM

The surface topography and the ferroelectric domain structures of the BFO nanoplates were studied by the PFM (Bruker, MultiMode-V with a Nanoscope controller V). AFM and PFM images were obtained in a contact mode with ambient conditions. The edge of the nanoplate was obtained by measuring the deflection error. The deflection error is interpreted as a derivative of topography and it can represent a fine change in height. An ac driving voltage of 2 V was applied to the Pt-coated Si conductive tip (MikroMasch, HQ:NSC35/Pt) at a typical scan speed of $\sim$5 μm s^{-1} with a frequency $\sim$10 kHz. All PFM images in this paper plot the real part piezoresponse signal [amplitude $\times$ cos(phase)]. In the VPFM images, the bright (dark) contrast indicates upward (downward) polarizations. In the LPFM images, the bright (dark) contrast represents the IP piezoresponse vector pointing to $+y(-y)$ when the head of the cantilever is oriented to the $-x$ direction. Owing to the asymmetric shape of the tip, the nanoplate in the PFM image is elongated to different directions depending on the direction of the cantilever. For the domain switching between ORQD and IRQD types, we applied dc $\pm$ 3 V to the tip with a scan speed of 5 μm s^{-1}.

C. c-AFM

Local conductivity properties were investigated by c-AFM (Bruker, MultiMode-V with a TUNA application module). It is possible to measure local conduction and surface topography simultaneously. The c-AFM images were performed using Pt-coated Si conductive tips (MikroMasch, HQ:NSC35/Pt) with a dc 1-V sample bias at a scan rate of $\sim$1 μm s^{-1}. We measured I-V curves with a voltage sweeping rate of 0.2 V s^{-1}. All the c-AFM data were acquired in ambient conditions and at room temperature. The current sensitivity setting of the c-AFM equipment was 10 pA V^{-1} and the typical noise level was $\sim$100 fA.

D. Phase field model

In the phase field model, we consider both polarization P and oxygen octahedral tilt θ as order parameters to describe

the Helmholtz free energy of BFO. Following previous work [41–43], the total free-energy density can be written as

$$F = \int_V \Big[\alpha_{ij} P_i P_j + \alpha_{ijkl} P_i P_j P_k P_l + \beta_{ij} \theta_i \theta_j + \beta_{ijkl} \theta_i \theta_j \theta_k \theta_l + t_{ijkl} P_i P_j \theta_k \theta_l + \frac{1}{2} g_{ijkl} \frac{\partial P_i}{\partial x_j} \frac{\partial P_k}{\partial x_l} + \frac{1}{2} k_{ijkl} \frac{\partial \theta_i}{\partial x_j} \frac{\partial \theta_k}{\partial x_l} + \frac{1}{2} c_{ijkl} \left(\varepsilon_{ij} - \varepsilon^0_{ij}\right)\left(\varepsilon_{kl} - \varepsilon^0_{kl}\right) - E_i P_i - \frac{1}{2} \epsilon_0 \kappa_b E_i E_j \Big] dV, \quad (2)$$

where α_{ij}, α_{ijkl}, β_{ij}, β_{ijkl}, and t_{ijkl} are the Landau polynomial coefficients, g_{ijkl} and k_{ijkl} are the gradient energy coefficients, x_i is the spatial coordinate, c_{ijkl} is the elastic stiffness tensor, ε_{ij} is the total strain, $\varepsilon^0_{ij} = h_{ijkl} P_k P_l + \lambda_{ijkl} \theta_k \theta_l + \varepsilon^{\text{lattice}}_{ij}$ is the eigenstrain where h_{ijkl} and λ_{ijkl} are the coupling coefficients and $\varepsilon^{\text{lattice}}_{ij}$ is the misfit strain caused by lattice parameter mismatch between BFO and the substrate, E_i is the electric field calculated from $E_i = -\partial\varphi/\partial x_i$ with φ the electrostatic potential, ϵ_0 is the permittivity of vacuum, and κ_b is the background relative dielectric constant. To figure out the elastic and electric driving forces for some certain polarization distribution, the mechanical equilibrium equations $\sigma_{ij,j} = 0$ and electrostatic equilibrium equation (Poisson equation) $D_{i,i} = \rho_f$ are solved, respectively, by using spectral iterative perturbation method [44]. Here, σ_{ij} is the local stress, and D_i is the electric displacement with ρ_f the density of free charges. Then, the temporal evolution of the order parameter is simulated by the time-dependent Ginzburg-Landau equations:

$$\frac{\partial P_i}{\partial t} = -L_p \frac{\delta F}{\delta P_i}, \quad \frac{\partial \theta_i}{\partial t} = -L_\theta \frac{\delta F}{\delta \theta_i}, \quad (3)$$

where L_p and L_θ are kinetic coefficients, and Eq. (3) is solved using the semi-implicit Fourier spectral method [45].

The whole system grid is $128\Delta x \times 128\Delta x \times 60\Delta x$ with $\Delta x = 0.5$ nm. It consists of three types of materials, i.e., $128\Delta x \times 128\Delta x \times 60\Delta x$ for substrate, $64\Delta x \times 64\Delta x \times 12\Delta x$ for BFO, and the rest of grids for air. The polarization in the air and substrate is set to be zero. The elastic stiffness in BFO and substrate is the same, while the elastic stiffness in air is zero. The misfit strain $\varepsilon^{\text{lattice}}_{ij}$ is determined by $\varepsilon^{\text{lattice}}_{ij} = (a_{\text{BFO}} - a_{\text{LAO}})/a_{\text{LAO}} = (3.965 - 3.821)/3.821 = 3.77\%$. In this phase field simulation, all coefficients are adopted from previous literature [41].

E. TEM

For the cross-sectional observation on the BFO nanoplate, the specimens were prepared by a dual-beam focused ion-beam system (JIB-4601F, JEOL, Japan). To protect the BFO plates and CFO films, an amorphous carbon layer was deposited on the top surface before ion-beam milling. A Ga^+ ion beam with an acceleration voltage of 30 kV was used to fabricate the thin TEM lamella. To minimize the surface damages induced by Ga^+ ion-beam milling, the sample was further milled with an Ar^+ ion beam (PIPS II, Gatan, USA) with an acceleration voltage of 0.8 kV for 15 min. Z-contrast HAADF STEM images were taken with a scanning transmission electron microscope (JEM-2100F, JEOL, Japan) at 200 kV with a spherical aberration corrector (CEOS GmbH, Germany). The optimum size of the electron probe was approximately 0.9 Å. The collection semiangles of the HAADF detector were adjusted from 80 to 220 mrad to exploit the large-angle elastic scattering of electrons for clear Z-sensitive images. The raw images obtained were processed with a Wiener filter with a local window to reduce background noise (HREM Research, Inc., Japan).

IV. CONCLUSION

In conclusion, we demonstrated that charged domain structures are stabilized in a BFO nanoplate subjected to radial strain relaxation. Significant electronic conduction appears in the vicinity of edges due to the accumulation of free carriers that compensate for polarization charges. From electrical poling experiments, we found that deterministic 180° polarization switching of the quadrant domains owing to the strain-gradient-induced protection of the ferroelastic domains can reverse the polarity of bound charges in the nanoplates. We demonstrated that the magnitude of conductivity can be manipulated in a reversible and nonvolatile manner. Phase field simulations reveal that the enhanced conductivity is caused by the interplay between polarization bound charges and junction space charges from the Schottky barrier. Our findings provide a concept to stabilize and manipulate charged domain structures for nanoelectronic applications.

ACKNOWLEDGMENTS

This work was supported by an NRF grant funded by the Korean Government via the Creative Research Initiative Center for Lattice Defectronics (Grant No. 2017R1A3B1023686) and the Center for Quantum Coherence in Condensed Matter (Grant No. 2016R1A5A1008184). This work was also supported by the Global Frontier Research and Development Program of the Center for Hybrid Interface Materials funded by the Ministry of Science, Information and Communication Technology and Future Planning (Grant No. 2013M3A6B1078872). The authors gratefully acknowledge financial support from the China Scholarship Council under Grant No. 201706190099 (Y.Z.) and from the National Key Project for Basic Research of China under Grant No. 2016YFA0300101 (J.M.L.). The work at The Pennsylvania State University was supported by the U.S. Department of Energy, Office of Basic Energy Sciences, Division of Materials Sciences and Engineering under Grant No. FG02-07ER46417 (F.X. and L.Q.C.) and by The Pennsylvania State University Materials Research Science and Engineering Center, Center for Nanoscale Science, under Grant No. NSF DMR-1420620 (F.X.).

[1] G. Catalan, J. Seidel, R. Ramesh, and J. F. Scott, Rev. Mod. Phys. **84**, 119 (2012).

[2] K.-E. Kim, B.-K. Jang, Y. Heo, J. H. Lee, M. Jeong, J. Y. Lee, J. Seidel, and C.-H. Yang, NPG Asia Mater. **6**, e81 (2014).

[3] N. Balke, M. Gajek, A. K. Tagantsev, L. W. Martin, Y.-H. Chu, R. Ramesh, and S. V. Kalinin, Adv. Funct. Mater. **20**, 3466 (2010).

[4] N. Balke, B. Winchester, W. Ren, Y. H. Chu, A. N. Morozovska, E. A. Eliseev, M. Huijben, R. K. Vasudevan, P. Maksymovych, J. Britson, S. Jesse, I. Kornev, R. Ramesh, L. Bellaiche, L. Q. Chen, and S. V. Kalinin, Nat. Phys. **8**, 81 (2012).

[5] T. Choi, Y. Horibe, H. T. Yi, Y. J. Choi, W. Wu, and S.-W. Cheong, Nat. Mater. **9**, 253 (2010).

[6] W. Wu, Y. Horibe, N. Lee, S.-W. Cheong, and J. R. Guest, Phys. Rev. Lett. **108**, 077203 (2012).

[7] T. Rojac, A. Bencan, G. Drazic, N. Sakamoto, H. Ursic, B. Jancar, G. Tavcar, M. Makarovic, J. Walker, B. Malic, and D. Damjanovic, Nat. Mater. **16**, 322 (2017).

[8] S. Farokhipoor and B. Noheda, Phys. Rev. Lett. **107**, 127601 (2011).

[9] C. Kittel, Phys. Rev. **70**, 965 (1946).

[10] I. I. Naumov, L. Bellaiche, and H. Fu, Nature (London) **432**, 737 (2004).

[11] C. M. Wu, W. J. Chen, Y. Zheng, D. C. Ma, B. Wang, J. Y. Liu, and C. H. Woo, Sci. Rep. **4**. 3946 (2014).

[12] D. Lee, A. Yoon, S. Y. Jang, J.-G. Yoon, J.-S. Chung, M. Kim, J. F. Scott, and T. W. Noh, Phys. Rev. Lett. **107**, 057602 (2011).

[13] B. C. Jeon, D. Lee, M. H. Lee, S. M. Yang, S. C. Chae, T. K. Song, S. D. Bu, J.-S. Chung, J.-G. Yoon, and T. W. Noh, Adv. Mater. **25**, 5643 (2013).

[14] G. Catalan, A. Lubk, A. H. G. Vlooswijk, E. Snoeck, C. Magen, A. Janssens, G. Rispens, G. Rijnders, D. H. A. Blank, and B. Noheda, Nat. Mater. **10**, 963 (2011).

[15] D. Lee, B. C. Jeon, A. Yoon, Y. J. Shin, M. H. Lee, T. K. Song, S. D. Bu, M. Kim, J.-S. Chung, J.-G. Yoon, and T. W. Noh, Adv. Mater. **26**, 5005 (2014).

[16] J. Seidel, L. W. Martin, Q. He, Q. Zhan, Y.-H. Chu, A. Rother, M. E. Hawkridge, P. Maksymovych, P. Yu, M. Gajek, N. Balke, S. V. Kalinin, S. Gemming, F. Wang, G. Catalan, J. F. Scott, N. A. Spaldin, J. Orenstein, and R. Ramesh, Nat. Mater. **8**, 229 (2009).

[17] R. K. Vasudevan, A. N. Morozovska, E. A. Eliseev, J. Britson, J.-C. Yang, Y.-H. Chu, P. Maksymovych, L. Q. Chen, V. Nagarajan, and S. V. Kalinin, Nano Lett. **12**, 5524 (2012).

[18] Z. L. Bai, X. X. Cheng, D. F. Chen, D. W. Zhang, L.-Q. Chen, J. F. Scott, C. S. Hwang, and A. Q. Jiang, Adv. Func. Mater. **28**, 1801725 (2018).

[19] J. Jiang, Z. L. Bai, Z. H. Chen, L. He, D. W. Zhang, Q. H. Zhang, J. A. Shi, M. H. Park, J. F. Scott, C. S. Hwang, and A. Q. Jiang, Nat. Mater. **17**, 49 (2018).

[20] N. Balke, S. Choudhury, S. Jesse, M. Huijben, Y. H. Chu, A. P. Baddorf, L. Q. Chen, R. Ramesh, and S. V. Kalinin, Nat. Nanotech. **4**, 868 (2009).

[21] A. Crassous, T. Sluka, A. K. Tagantsev, and N. Setter, Nat. Nanotech. **10**, 614 (2015).

[22] R. K. Vasudevan, Y. Matsumoto, X. Cheng, A. Imai, S. Maruyama, H. L. Xin, M. B. Okatan, S. Jesse, S. V. Kalinin, and V. Nagarajan, Nat. Commun. **5**, 4971 (2014).

[23] L. You, Z. Chen, X. Zou, H. Ding, W. Chen, L. Chen, G. Yuan, and J. Wang, ACS Nano **6**, 5388 (2012).

[24] S. H. Baek, H. W. Jang, C. M. Folkman, Y. L. Li, B. Winchester, J. X. Zhang, Q. He, Y. H. Chu, C. T. Nelson, M. S. Rzchowski, X. Q. Pan, R. Ramesh, L. Q. Chen, and C. B. Eom, Nat. Mater. **9**, 309 (2010).

[25] S. V. Kiselev, R. P. Ozerov, and G. S. Zhdanov, Sov. Phys. Dokl. **7**, 742 (1963).

[26] Y. E. Roginskaya, Y. Y. Tomashpol'skiĭ, Y. N. Venevtsev, V. M. Petrov, and G. S. Zhdanov, Sov. Phys. JETP **23**, 47 (1966).

[27] D. H. Kim, H. N. Lee, M. D. Biegalski, and H. M. Christen, Appl. Phys. Lett. **92**, 012911 (2008).

[28] H. Zheng, J. Wang, S. E. Lofland, Z. Ma, L. Mohaddes-Ardabili, T. Zhao, L. Salamanca-Riba, S. R. Shinde, S. B. Ogale, F. Bai, D. Viehland, Y. Jia, D. G. Schlom, M. Wuttig, A. Roytburd, and R. Ramesh, Science **303**, 661 (2004).

[29] See Supplemental Material at http://link.aps.org/supplemental/10.1103/PhysRevMaterials.2.084412 for x-ray-diffraction study, details of quadrant domain structure, I-V curves plotted within the framework of a Schottky emission model, and phase field simulations of electronic conductivity.

[30] K. Chu, B.-K. Jang, J. H. Sung, Y. A. Shin, E.-S. Lee, K. Song, J. H. Lee, C.-S. Woo, S. J. Kim, S.-Y. Choi, T. Y. Koo, Y.-H. Kim, S.-H. Oh, M.-H. Jo, and C.-H. Yang, Nat. Nanotech. **10**, 972 (2015).

[31] K.-E. Kim, S. Jeong, K. Chu, J. H. Lee, G.-Y. Kim, F. Xue, T. Y. Koo, L.-Q. Chen, S.-Y. Choi, R. Ramesh, and C.-H. Yang, Nat. Commun. **9**, 403 (2018).

[32] T. K. Ghanem, E. D. Williams, and M. S. Fuhrer, J. Appl. Phys. **110**, 054305 (2011).

[33] Y.-H. Hsieh, E. Strelcov, J.-M. Liou, C.-Y. Shen, Y.-C. Chen, S. V. Kalinin, and Y.-H. Chu, ACS Nano **7**, 8627 (2013).

[34] D. W. Reagor, S. Y. Lee, Y. Li, and Q. X. Jia, J. Appl. Phys. **95**, 7971 (2004).

[35] H. B. Michaelson, J. Appl. Phys. **48**, 4729 (1977).

[36] C. Wang, K.-J. Jin, Z.-T. Xu, L. Wang, C. Ge, H.-B. Lu, H.-Z. Guo, M. He, and G.-Z. Yang, Appl. Phys. Lett. **98**, 192901 (2011).

[37] J. Seidel, P. Maksymovych, Y. Batra, A. Katan, S.-Y. Yang, Q. He, A. P. Baddorf, S. V. Kalinin, C.-H. Yang, J.-C. Yang, Y.-H. Chu, E. K. H. Salje, H. Wormeester, M. Salmeron, and R. Ramesh, Phys. Rev. Lett. **105**, 197603 (2010).

[38] B. S. Holinsworth, D. Mazumdar, H. Sims, Q.-C. Sun, M. K. Yurtisigi, S. K. Sarker, A. Gupta, W. H. Butler, and J. L. Musfeldt, Appl. Phys. Lett. **103**, 082406 (2013).

[39] S. Hong, S. Tong, W. I. Park, Y. Hiranaga, Y. Cho, and A. Roelofs, Proc. Natl. Acad. Sci. USA **111**, 6566 (2014).

[40] L. Li, J. Britson, J. R. Jokisaari, Y. Zhang, C. Adamo, A. Melville, D. G. Schlom, L.-Q. Chen, and X. Pan, Adv. Mater. **28**, 6574 (2016).

[41] F. Xue, Y. Gu, L. Liang, Y. Wang, and L.-Q. Chen, Phys. Rev. B **90**, 220101 (2014).

[42] F. Xue, Y. Li, Y. Gu, J. Zhang, and L.-Q. Chen, Phys. Rev. B **94**, 220101 (2016).

[43] F. Xue, L. Li, J. Britson, Z. Hong, C. A. Heikes, C. Adamo, D. G. Schlom, X. Pan, and L.-Q. Chen, Phys. Rev. B **94**, 100103 (2016).

[44] J. X. Zhang, R. Wu, S. Choudhury, Y. L. Li, S. Y. Hu, and L. Q. Chen, Appl. Phys. Lett. **92**, 122906 (2008).

[45] L. Q. Chen and J. Shen, Comput. Phys. Commun. **108**, 147 (1998).